

A Monte Carlo based method for the dynamic “fragility analysis” of tall buildings under turbulent wind loading

Marra A. Smith, Luca Caracoglia *

Department of Civil and Environmental Engineering, Northeastern University, Boston, MA 02115, USA

ARTICLE INFO

Article history:

Received 31 July 2009

Received in revised form

1 October 2010

Accepted 21 October 2010

Available online 20 November 2010

Keywords:

High-rise buildings

Wind loading

Along-wind dynamic response

Monte Carlo simulation

CAARC building

Performance-based assessment

ABSTRACT

This paper presents a numerical algorithm for the simulation of the along-wind dynamic response of tall buildings under turbulent winds, using Monte Carlo (MC) integration methods. The proposed MC numerical procedure was used to compute the power spectral density of the buffeting loads, and to derive the statistics of the dynamic response in the presence of uncertainty in the wind loading. The CAARC prototype building was utilized to validate the proposed algorithm. This paper also presents the computation of the structural fragility curves of the CAARC building under extreme winds; preliminary investigations were conducted to assess the applicability of the proposed algorithm to a performance-based assessment.

The results of these studies validated the appropriateness of the developed algorithm through comparison to reference values obtained from the literature for the CAARC building. Furthermore, structural “fragility curves” were utilized for a preliminary performance analysis, based on simulated along-wind response serviceability limit states.

© 2010 Elsevier Ltd. All rights reserved.

1. Introduction

Comprehensive research activities in the recent past have been undertaken in the area of risk-based assessment of structural integrity with a specific focus on earthquake engineering (performance-based engineering, PBE) [1]. In PBE, the basic idea is to ensure that a structure, for example, subjected to different levels of hazards (as opposed to the largest foreseeable event), is capable of achieving a selected performance objective level [2]. The overall concept of PBE provides an attractive alternative for owners, since it can enable cost-effective design and can reduce planning in the aftermath of a catastrophic event.

PBE was introduced in the late 1960s as part of the “Operation Breakthrough Project” [3]; in 1977 reliability-based criteria for strength and serviceability limit states against earthquake hazards were first published [4]. Recently, there has been a renewed interest towards this method, especially for earthquake-resistant design, as a consequence of the advances in computer-based structural analysis [5]. The Structural Engineers Association of California (SEAOC) [3] set about to design structures based on a correlation between earthquake recurrence intervals and performance levels in their “Vision 2000” project [6,7], in

which performance levels were combined with excitation levels to determine appropriate design criteria. Other examples of publications for the PBE-oriented seismic design include ATC 33, FEMA 273 (later replaced by FEMA 356), ATC 40 [6] and other recommendations by SEAOC [8].

In wind engineering the need for random vibration, spectral-based and peak-estimation methods has been recognized since the early stages of the research activities on high-rise buildings (e.g., [9–12]), due to the presence of random turbulence in the loading and dynamic vibration of the structure. Nevertheless, less emphasis has been devoted to a systematic investigation of the applicability of PBE concepts to the analysis of wind hazards, especially for tall buildings [6,13–15], for which dynamic vibration is of relevance for serviceability design. Even though risk-based methods for seismic design are readily available to practicing engineers, a “technology transfer” to wind hazards is not directly possible due to the uniqueness of the excitation mechanism, associated with turbulence. A literature review of recent applications of PBE in wind engineering has revealed that most research has been directed towards a more efficient design of low-rise buildings [2,16,17], where damage and collapse can be related to localized loss of capacity in key members or connections. Few studies are available on high-rise buildings, in which either a framework for the analysis of uncertainty has been developed [13,18], or in which a methodology for the design of buildings has been proposed [6,15].

This paper discusses the preliminary results of an ongoing research activity, which is oriented towards the development of

* Corresponding address: Department of Civil and Environmental Engineering, Northeastern University, 400 Snell Engineering Center, 360 Huntington Avenue, Boston, MA 02115, USA. Tel.: +1 617 373 5186; fax: +1 617 373 4419.

E-mail address: lucac@coe.neu.edu (L. Caracoglia).

Notations

B	building width
C_D	drag coefficient per unit length
C_L	lift coefficient per unit length
C_z	exponential decay coefficient
D	building depth
f	reduced frequency
f_{V_z}	PDF of reference wind speed
$\hat{f}(n, z_1, z_2)$	surface integral
$F(z, t)$	wind force per unit length
F_T	structural response fragility
g	mode designation
h	building height
I_u	longitudinal turbulence intensity
I_v	lateral turbulence intensity
k	tolerance factor of normal distribution
$m(z)$	simulated mass per unit length
M_{gg}	modal mass (mode g)
n	natural frequency
n_p	number of data points in a sample
n_0	fundamental natural frequency
N_{MC}	number of Monte Carlo integration points
P	probability
P_T	probability of “performance loss”
s_n	sample standard deviation
$S_u(n, z)$	longitudinal turbulence spectrum
T	pre-selected threshold
$u(z, t)$	turbulence component of wind velocity (x -direction)
$\bar{U}(z)$	mean component of wind velocity
$v(z, t)$	turbulence component of wind velocity (y -direction)
V_z	mean wind velocity ($V_z = \bar{U}(h)$ at $z = h$)
\bar{x}_σ	mean of sample
$x(z, t)$	dynamic displacement (x -direction)
X	generic random variable
\bar{X}	mean or static response
$y(z, t)$	dynamic displacement (y -direction)
z	elevation
z_0	roughness length
z_1, z_2	integration variables in Eq. (1)
z^*	represents the extent of the normal distribution
Z_0	lower bound integration limit in Eq. (5)
Z_A, Z_B	upper bound integration limit in Eq. (5)
α	incidence angle of the mean wind
ζ_{aero}	aerodynamic damping
ζ_{st}^*	structural damping
μ	true value of population mean
$\xi_g(t)$	dynamic generalized coordinate of displacement (mode g)
ρ	air density
σ_x	RMS response in x -direction
$\Phi_g(z)$	mode shape (mode g)

a performance-based methodology for wind engineering analyses with an application to tall buildings. As part of these investigations, a numerical method for estimating the dynamic response of a high-rise structure due to buffeting loads is discussed. The significance of this approach is related to the possibility of replicating the “closed-form” analytical methods, based on random vibration techniques in the frequency domain, through equivalent numerical Monte Carlo (MC) algorithms. Even though MC methods are routinely employed by researchers and engineers for uncertainty propagation estimation (e.g., [19–21]), the main contribution of this study is associated with the development of a computationally

efficient “two-step MC algorithm”, capable of assessing the along-wind dynamic response of a tall building, which also incorporates uncertainty in the loading. The proposed numerical algorithm enables the statistical assessment of the response for a set of “uncertain loading scenarios”, which simulate the presence of modeling simplifications and measurement errors. Such errors can arise during a wind tunnel test, in which a reduced-scale model is employed to estimate the prototype response. As an example, the proposed algorithm might possibly be employed to statistically derive the dynamic response of a building during a “high-frequency force balance” experiment, when corrections of the wind tunnel experimental data are required to account for complex three-dimensional mode shapes in the prototype structure (e.g., [22–25]).

In the second part of the study, a preliminary application of the proposed algorithm is presented in an example. The statistical characterization of comfort criteria for a simulated tall office building, located near Boston, Massachusetts, United States, is discussed. Recent studies have shown in fact that the selection of comfort criteria has a significant role in the design of tall buildings, since motion can cause occupants to experience extreme discomfort [13,26–30]. The comfort of the occupants was related to pre-selected performance levels, based on the estimation of along-wind vibration at the top floor, simulated through the proposed numerical algorithm. Even though acceleration has been usually preferred as a descriptor of comfort performance in tall buildings [13,26–30], maximum lateral displacements were considered in this study; results should be therefore interpreted as preliminary, requiring further investigation prior to implementation of the algorithm.

2. Proposed methodology

The proposed methodology utilizes standard frequency-domain random-vibration analysis for the estimation of wind-induced loading and dynamic response on a high-rise building [10,12,31]. The procedure assumes that the dynamic behavior of the structure under consideration was linear-elastic. This assumption was valid since, at the present stage, investigations were primarily concentrated on serviceability limit states. In these cases, modal superposition was used to capture the main dynamic response [31,32].

The simplified building, considered herein, has a prismatic floor plan and a main wind force resisting system composed of lateral frames, which are symmetrically located with respect to the primary axes of bending of the global structure. Torsional effects were assumed of secondary relevance [33] since the main objective of the simulations was the validation of the proposed numerical procedure.

The proposed approach was employed to analyze the dynamic response at large wind velocities, for which dynamic buffeting response is the main concern. The aerodynamic loading was based on equivalent quasi-steady formulation of wind forces [10,12,31]. Mean direction of the incident wind was considered orthogonal to one of the vertical faces of the building. The static torsional moment coefficient, per unit height of the structure (assessed by integrating pressures over the surface of the building), and its first derivative were neglected to restrict the dynamic response principally in the along-wind direction. Load induced by vortex shedding was also neglected in this preliminary investigation, as vortex shedding is primarily considered of importance at lower wind velocities, and is considered less critical for displacements as opposed to accelerations [12,34].

Fig. 1 is a schematic depicting building and axis orientation, wind loading, $F_d(z, t)$, per unit height z , and bending displacements as a result of dynamic response. The dynamic displacements

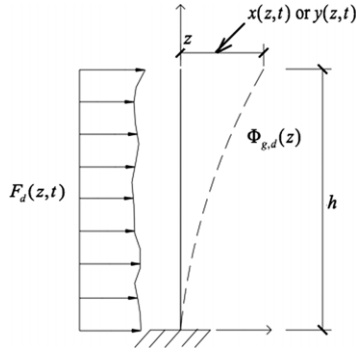


Fig. 1. Schematic of building orientation, loading, and displacements.

are denoted as $x(z, t)$ and $y(z, t)$ for the along-wind and across-wind dynamic response, respectively. The static response in the along-wind direction (not shown in the figure) is denoted as $\bar{X}(z)$. The normalized mode shape of the generic mode g , which is not necessarily a linear function of the vertical coordinate z , is denoted by $\Phi_{g,d}(z)$, with the subscript $d = x$ indicating the along-wind response and $d = y$ indicating the across-wind response; the mean wind incidence angle is assumed as α . The general equation of the total dynamic response in the along-wind direction, in the case that multiple structural modes are considered, can be derived by modal superposition as $x(z, t) = \sum \Phi_{g,x}(z) \xi_{g,x}(t)$, with $\xi_{g,x}(t)$ being the generalized coordinate of mode g .

The main equations for the evaluation of the dynamic response for the along-wind direction in the frequency domain are summarized below:

$$\begin{aligned} S_{Qg,xQg,x}(n) &= \rho^2 B^2 \int_0^h \int_0^h [C_D \Phi_{g,x}(z_1) \Phi_{g,x}(z_2) \bar{U}(z_1) \bar{U}(z_2) S_{uu}(n, z_1, z_2)] dz_1 dz_2 \\ &= \rho^2 B^2 \int_0^h \int_0^h [\hat{f}(n, z_1, z_2)] dz_1 dz_2 \end{aligned} \quad (1)$$

$$S_{uu}(n, z_1, z_2) = \sqrt{S_{uu}(n, z_1) S_{uu}(n, z_2)} \exp \left(n \frac{\sqrt{C_z^2 (z_1 - z_2)^2}}{0.5(\bar{U}(z_1) + \bar{U}(z_2))} \right) \quad (2)$$

$$\begin{aligned} S_{xx}(z, n) &\cong \sum_g \frac{\Phi_{g,x}(z) \Phi_{g,x}(z) S_{Qg,xQg,x}(n)}{M_{gg,x}^2 (2\pi n_{0g,x})^4 \left[\left(1 - \frac{n^2}{n_{0g,x}^2} \right)^2 + \left(2 \frac{n}{n_{0g,x}} \right)^2 (\zeta_{stg,x}^* + \zeta_{aerog,x})^2 \right]} \end{aligned} \quad (3)$$

$$\sigma_x(z) = \sqrt{\int S_{xx}(z, n) dn}. \quad (4)$$

Eq. (1) corresponds to the modal force spectra as a function of frequency, n , with C_D being the drag coefficient per unit vertical length, normalized with respect to the B dimension of the building (Fig. 2), measured for $\alpha = 0$. The mean wind velocity is denoted by $\bar{U}(z)$, while the height of the building by h . Eq. (2) is the cross-spectrum of the along-wind turbulence, u , at z_1 and z_2 , where $S_{uu}(n, z)$ is the longitudinal velocity spectrum. The quantity C_z is an exponential decay coefficient [35], which is a quasi-steady measure of the partial loss of coherence in the vertical direction of the pressure loading induced by turbulence [31]. Eq. (3) describes the response auto-spectra without modal cross-coupling. In Eq. (3), $\zeta_{stg,x}^*$ is the structural damping coefficient, $\zeta_{aerog,x}$ is the aerodynamic damping [35], and $M_{gg,x}$ is the modal mass. Eq. (4) describes the root mean square (RMS) response, derived from Eq. (3).

The previous equations assume that the response in the x -direction and the y -direction is dominated by the two fundamental and mutually orthogonal bending modes ($g = 1$) with mode shapes $\Phi_{1,x}(z)$ and $\Phi_{1,y}(z)$. Structural and aerodynamic coupling was neglected at this time between the x -direction and the

y -direction components. Even though the results will not be presented in this paper, additional simulations were conducted to determine the potential influence of modal aerodynamic coupling between the two primary bending planes [35,36].

Effects of uncertainty in the characterization of aerodynamic loading and their influence on the dynamic response were simulated through MC algorithms. In this study uncertainty associated with modeling and experimental errors was simulated by appropriate random perturbation applied to some of the parameters in Eqs. (1)–(4), such as C_z or C_D , about a reference deterministic value. The proposed methodology utilizes MC methods to accomplish the following steps: (1) compute the power spectral density of the modal buffeting force (Eq. (1)) as a function of frequency, restricted to $g = 1$ in the following examples, by numerical integration; and (2) derive statistical information about the dynamic response when uncertainty in the characterization of dynamic loading is accounted for. By combining Steps 1 and 2, a “Two-Step Monte Carlo Algorithm” was developed and implemented to estimate the along-wind dynamic response of a high-rise building.

The two-step MC procedure enabled the numerical calculation of a generic surface integral, $\hat{f}(n, z_1, z_2)$, being the function enclosed within brackets in Eq. (1) and corresponding to the modal spectral loading. This surface integral was evaluated by utilizing a set of randomly generated and uniformly distributed numbers (integration points) to numerically estimate the statistical expectation of the function $\hat{f}(n, z_1, z_2)$ [19]. In the case of the double integral, there are two randomly generated samples of size N_{MC} defined on the intervals $[Z_0, Z_A]$ and $[Z_0, Z_B]$, where the variables $Z_0 = 0$, $Z_A = h$ and $Z_B = h$ are the integration limits along the height of the structure. The following equation gives the general form of the equation used to approximate the double integral in Eq. (1) with integrand $\hat{f}(n, z_1, z_2)$:

$$\begin{aligned} \int_{Z_0}^{Z_A} \int_{Z_0}^{Z_B} \hat{f}(n, z_1, z_2) dz_1 dz_2 \\ \cong E[\hat{f}(n, z_1, z_2)](Z_A - Z_0)(Z_B - Z_0). \end{aligned} \quad (5)$$

The previous equation would be exact if the estimation of the expectation $E[\hat{f}(n, z_1, z_2)]$ were based on an infinite sample. Since the assessment of $E[\hat{f}(n, z_1, z_2)]$ relies on arithmetic averaging (practically), the right-hand side of the integral is approximate [19]. Therefore, the inequality sign was employed in Eq. (5) because the assessment of expectation is inexact.

3. Description of the simulated building (CAARC)

The “CAARC building” was analyzed as a prototype structure. This example was originally selected by the Commonwealth Advisory Aeronautical Research Council of Australia in 1980 as a benchmark high-rise structure to be employed for studying its wind-induced dynamic response [37]. The full-scale building is a prismatic structure with a rectangular floor plan of dimensions $B = 30.5$ m and $D = 45.7$ m. Fig. 2(a) shows a schematic of the CAARC building with an indication of the main dimensions (depth D , width B , height h); Fig. 2(b) shows a horizontal plane view indicating the wind directionality, corresponding to a zero incidence angle of the wind, α .

Table 1(a,b) summarizes the CAARC building full-scale model parameters that were employed in the simulations. The dynamic response, numerically evaluated by this study, was compared with the original experimental results from wind-tunnel-based aeroelastic models, tested in a series of laboratories [37]. First-mode dynamic response of the prototype building in the along-wind (Eq. (2)) and across-wind directions were simulated by considering the information described in [37]. Data, summarized

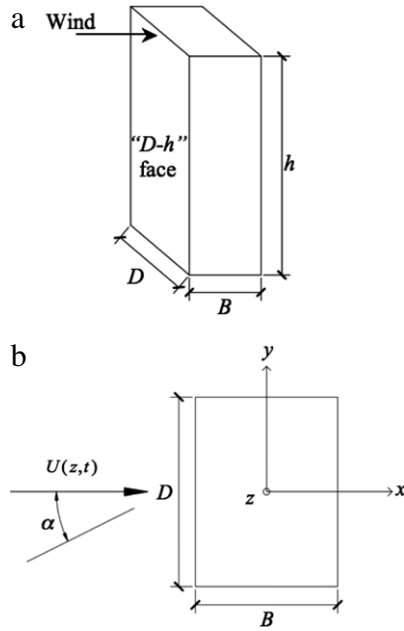


Fig. 2. (a) Schematic view of the CAARC building; (b) schematic of building orientation and wind directionality (horizontal plane view).

Table 1
CAARC Building – (a) Numerical model parameters; (b) wind loading parameters [37].

(a) Variable	Value assigned
h (m)	183
dz (m) Eq. (1)	1
$m(z)$ (kg/m)	220,800
$\zeta_{st1,x}^* = \zeta_{st1,y}^* (g = 1)$	0.01
$n_{01,x} = n_{01,y} = n_0$ (Hz)	0.2
$\Phi_{1,x}(z) = \Phi_{1,y}(z)$	$(z/h)^\gamma; \gamma = 1$
Z_0 (m)	0
$Z_A = Z_B$	h
(b) Variable	Value assigned
ρ (kg/m ³)	1.25
Roughness, z_0 (m) ^a	0.5
$\bar{U}(z)$ (m/s)	$\bar{U}(h)(z/h)^\beta; \beta = 0.25$
$I_u(z)$ ^b	$-0.055(z/h) + 0.1533$
$I_v(z)$	$0.75I_u(z)$
$C_{z,u}$	10
$C_{z,v}$	$0.667C_{z,u}$
C_D	1
C_L	–0.1
$dC_D/d\alpha$	–1.1
$dC_L/d\alpha$	–2.2

^a Estimated from wind tunnel [37].

^b Derived from wind tunnel measurements; Fig. 2 in [37].

in Table 1(a) and Table 1(b), were either directly derived or inferred from the figures and tables in [37]. Table 1(a) includes structural, geometric properties of the building while Table 1(b) shows the main characteristics of the simulated boundary layer wind, required by Eq. (2). As outlined in Section 2, quasi-steady pressure loading, based on mean wind force and fluctuating turbulence components u and v (Eqs. (1)–(4)), was utilized. Coupling in the two primary planes of bending, influenced by either a three-dimensional spatial configuration of the mode shapes or the aerodynamics (e.g., cross-correlation of turbulence components u and v), was not considered.

In Table 1(a) the building mass per unit length, $m(z)$, structural frequencies, and modal damping were calibrated to replicate the full-scale prototype response; fundamental bending modes in the

x (along wind) and y (across wind) directions were assumed as purely flexural, with mode shapes $\Phi_{g,x}(z)$ and $\Phi_{g,y}(z)$ ($g = 1$) oriented along the planes z – x and z – y and linearly varying with (z/h) ; three-dimensional dynamic response and influence of torsion were neglected.

In Table 1(b) the wind loading was simulated by replicating the boundary layer features (e.g., mean wind profile and turbulence characteristics), simulated in the wind tunnel, which were employed by all participating laboratories in [37]. For example, turbulence intensities (Table 1(b)) in the direction parallel to the B side (along-wind, u) and parallel to the D side (across-wind, v) were derived by calibration of the values employed in [37] to possibly replicate the full-scale behavior. In the absence of more detailed information in [37], a reduction of the turbulence intensity, I_v , in comparison with I_u was postulated [38], as shown in Table 1(b).

The longitudinal turbulence spectrum, employed by Eq. (2) to represent the stationary time-dependent dynamic loading, was derived by fitting an experimental dimensionless spectrum, derived from the tests in [37], as indicated below in Eq. (6a), with f being a reduced frequency (Eq. (6b)):

$$\frac{nS_{uu}(n)}{\bar{U}(h)^2 I_u^2} = \frac{0.6f}{(2 + f^2)^{5/6}} \quad (6a)$$

$$f = \frac{1600n}{\bar{U}(h)}. \quad (6b)$$

Static coefficients of lift and drag (C_D , C_L) and their first derivatives per unit length (employed for turbulence-induced across-wind response, not shown in Eqs. (1)–(4)) were exclusively considered. Reference values of C_D , C_L , etc. (Table 1(b)) were obtained by averaging the experimental data of mean surface pressure coefficients, acquired from the pressure taps installed on the wind tunnel models in [37] around the external surface. In this study, C_D and C_L were considered independent of height and were referenced to a strip of unit height taken at approximately two-thirds of the total h . Even though these values were held constant along the z direction for initial simulation purposes, the algorithm readily allows for the parameters to locally vary with z . Finally, any eccentricity in the wind loading was neglected, which was plausible for mean wind incidence angle $\alpha = 0$ with direction orthogonal to the “ $D - h$ ” face in Fig. 2.

4. Numerical validation

The purpose of this set of simulations was two-fold: (1) verification and updating of the model and wind loading parameters in Table 1 to be compatible with the wind tunnel response in [37]; (2) validation of the first step of the proposed MC algorithm through optimal selection of the number of MC integration points.

4.1. Closed-form validation and preliminary investigations

The “closed-form” (CF) numerical solution was compared to wind tunnel based reference values. The CF solution employed a discrete integration scheme for the derivation of the modal force. The modal force was subsequently utilized to determine a reference dynamic RMS response of the building at the top floor, $z = h$, after integration of the power spectral density of the response, frequency by frequency (Eq. (1)).

An example of the results is shown in Fig. 3, in which the CF numerical solution of the RMS response in the along-wind direction is compared to wind tunnel measurements, as a function of the reduced velocity, $\bar{U}(h)/(n_0 B)$. The building response was normalized with respect to the dimension B , the frequency of the first bending mode n_0 , and the mean velocity at h . Excellent

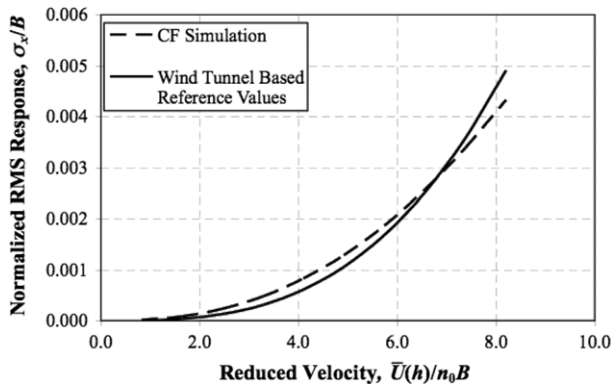


Fig. 3. Comparison of “closed-form” (CF) numerical simulation to the CAARC building response derived from wind tunnel tests [37] for wind orthogonal to the “D – h” face in Fig. 2.

correspondence was found, as evident from the analysis of this figure, with an absolute error no more than two percent between the two curves. Similar results, not shown for brevity, were observed in the case of the mean wind response, while some discrepancy was seen when the comparison was extended to the across-wind direction. This discrepancy was attributed, in part, to the effects of vortex shedding (not simulated by the current wind loading model), and to a less reliable derivation of the derivative of the lift static coefficient because of the lack of pressure data for wind incidence angles in the proximity of $\alpha = 0$ in [37]. Furthermore, this result also justified the use of the CF numerical simulation results as “exact” target values, i.e., as the reference for comparison with the approximate integration scheme introduced by the MC algorithm (Eq. (5)).

4.2. Validation of the MC algorithm

The functionality of the MC integration algorithm (second objective of the validation study) was assessed through repeated numerical estimation of the integral in Eq. (1) and through comparison to the CF value in the absence of uncertainty propagation with Eq. (5), i.e., a standard buffeting analysis. Fig. 4 shows the main results of this study. Fig. 4(a) depicts the “scatter plot” of the RMS dynamic response at the top of the building (Eq. (5)), associated with 100 consecutive numerical evaluations of the integral in Eq. (1) through MC simulation as a function of the random sample size (N_{MC}). Since the assessment of the expectation in Eq. (5) is carried out by arithmetic averaging and is based on a finite sample of the integration domain through N_{MC} random points, the “integral estimator” in Eq. (5) consequently becomes a random variable. Therefore, each point in Fig. 4(a) corresponds to a (random) realization of the MC-based integral estimator and depends on the choice of N_{MC} .

In Fig. 4(a) the normalized along-wind RMS response of the top floor of the CAARC building, computed by the MC method at reduced velocity $\bar{U}(h)/(n_0B) = 8.2$, is compared to the “exact” CF value (see Fig. 3). As expected, larger deviations and variability from the CF value can be observed when a smaller number of sampling points (N_{MC}) is employed. The maximum absolute error is variable between 7% for $N_{MC} = 1000$ and 2% for $N_{MC} = 10,000$, while it is almost negligible for larger sample sizes. The coefficient of variation (CoV), calculated for each sample population and variable N_{MC} , was employed as a statistical indicator for the selection of an “optimal” N_{MC} value (Fig. 4(b)). As shown in Fig. 4(b), the CoV was very small, generally less than 2% in all cases, and almost negligible for N_{MC} beyond 10,000. Even though a progressive reduction in the CoV was observed as N_{MC}

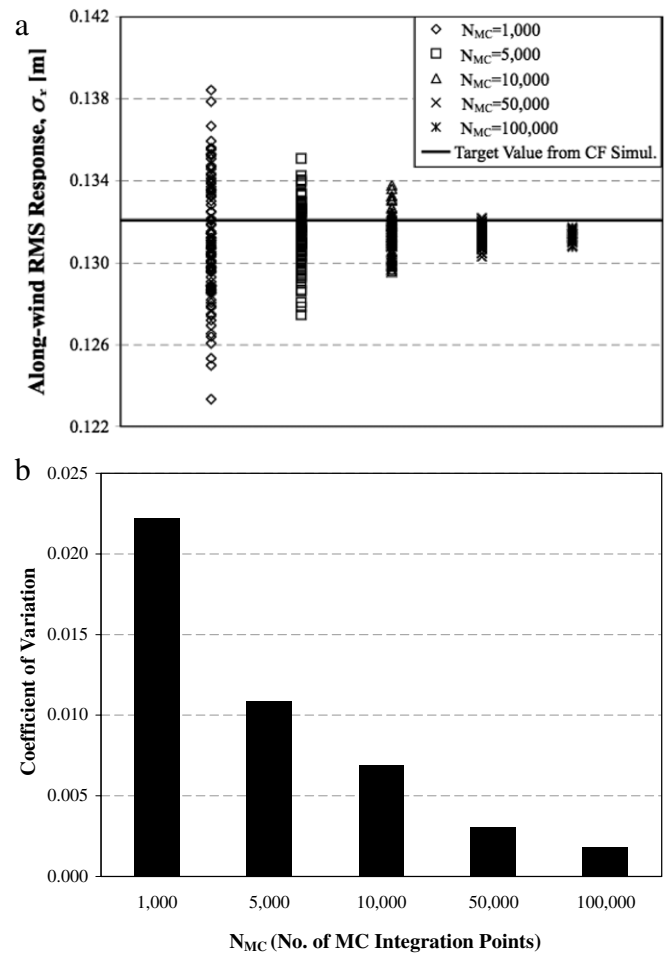


Fig. 4. Normalized along-wind RMS response of the CAARC building at $\bar{U}(h)/(n_0B) = 8.2$, computed by MC method (Step 1) – (a) scatter plot of 100 consecutive MC simulations as a function of the No. of MC integration points (N_{MC}); (b) coefficient of variation vs. N_{MC} .

increased, the decrement was not proportional to the number of integration points.

Other studies were conducted, and the results were employed to assist in the selection of the “optimal” N_{MC} value; indicators included the estimator bias, tolerance intervals and confidence intervals. The results from each of these studies are presented in Table 2. The estimator bias is the difference between the expected value of the estimator and the true value of the quantity that is being estimated. In this case, it is the difference between the “exact” target value (CF) and the arithmetic mean of the sample, denoted by \bar{x}_σ . In Table 2 the bias for $N_{MC} = 1000$ is considerably larger than the one obtained for any other sample size. Similarly, for large values of N_{MC} , the bias appears to increase in comparison with the recorded error, especially for $5000 < N_{MC} < 10,000$.

A second investigation employed the concepts of confidence intervals and tolerance intervals. The confidence interval is used to estimate the population mean based on experimentally observed data. The equation $\mu = \bar{x}_\sigma \pm (z^*s_n/\sqrt{n_p})$ was used to calculate the “large-sample confidence interval” [39], in which μ is the true value of the population mean, \bar{x}_σ is the sample mean (the MC estimator), s_n is the sample standard deviation, z^* is a dimensionless value representing the extent of the normal distribution with a given probability, and n_p is the number of data points that are sampled (i.e., $n_p = 100$). The confidence interval, defined above, was utilized to estimate the upper and lower bounds of the exact population mean from the sample mean, for a degree of confidence equal to 95% with $z^* = 1.96$ [39].

Table 2Results of various validation studies conducted on the CAARC building to determine the sample size, N_{MC} .

N_{MC}	Bias $\times 10^{-3}$ ($\sigma_{x,target} - \bar{x}_\sigma$)	Relative width of tolerance interval ^a	Maximum relative error for confidence interval ^b (%)	Minimum relative error for confidence interval ^b (%)
1000	1.00	10.1	1.19	0.32
5000	0.64	5.0	0.70	0.27
10,000	0.66	3.1	0.64	0.37
50,000	0.77	1.4	0.65	0.53
100,000	0.74	1.0	0.63	0.49

^a Interval length relative to interval length at $N_{MC} = 100,000$.^b Error relative to CF target value.

Subsequently, calculations were performed to find the tolerance intervals for each set of data points. Tolerance intervals were employed since they are related to the definition of a broader interval, in which each single observation of the MC integral estimator might be located [39]. This second analysis was relevant to the algorithm because the modal integral associated with Step 1 (Eq. (5)) is evaluated only once, and is not derived from the average, \bar{x}_σ . It is important that a single MC-based estimation of the integral of the modal force PSD in terms of frequency (n) outputs a result as close to the “exact” value as possible. In the evaluation of the tolerance limits of the Step 1 integral, a normal distribution for the estimator was considered acceptable. In the absence of the true values for the mean and standard deviation of the population [39], the following relationship was employed: $\bar{x}_\sigma \pm k s_n$. The quantity k (tolerance factor for a normal distribution [39]), was selected in this study such that there was a 99% confidence that the calculated tolerance limits would contain at least 95% of the measurements; this corresponds to $k = 2.36$ [39].

A summary of confidence and tolerance results for the CAARC building as a function of N_{MC} can be found in Table 2. As anticipated, the tolerance interval was always larger than the confidence interval. The investigation also showed a correlation between the number of integration points, N_{MC} , and the tolerance intervals, suggesting a reduction of tolerance bounds as N_{MC} increases. For example, the tolerance interval of the top-floor RMS response at $\bar{U}(h)/(n_0 B) = 8.2$ is approximately 10 times longer for $N_{MC} = 1000$ than it is for $N_{MC} = 100,000$. For this structure, the benefit of using more integration points is clearly shown. Nevertheless, Table 2 also suggests that as the tolerance interval decreases, the bias error may on occasion increase for a larger N_{MC} . The latter remark seems partially contrasting against the observation that a larger sample size might be preferable, since a reduction in the bias error should be anticipated. It is believed that the perceived increment at larger N_{MC} could possibly be influenced by the definition of the target RMS response, employed in this study, i.e., related to the assessment of the integral in Eq. (2) in “closed form”, which was still derived by numerical integration. Influence of numerical tolerance on the CF value and, consequently, a marginal effect on the relative error estimation for very small bias (e.g., for $N_{MC} > 50,000$ in Table 2), cannot be excluded.

Therefore, the decision on an “optimal” N_{MC} value was based on a compromise between bias and tolerance in Table 2. In an attempt to consider both aspects at the same time, the maximum absolute and relative errors between the CF value and the sample mean of the MC integral estimator were also considered.

The run time of the algorithm was also analyzed as a supplemental indicator of algorithmic performance. Table 3 summarizes the effects of N_{MC} on the run time of the MC algorithm. Values were normalized with respect to the time for $N_{MC} = 100,000$, and were compared to the relative time coincident with the CF simulation. Benefits of the MC integration are evident from the table (reduction of computational time by a factor of 100).

By combining all the results from Fig. 4 and Tables 2 and 3, the “optimal” number of integration points for the CAARC building

Table 3MC validation: run time vs. number of integration points (N_{MC}).

N_{MC}	Average relative run time ^a
1000	0.002
5000	0.012
10,000	0.024
50,000	0.265
100,000	1.000
Closed-Form	2.775

^a Run time relative to $N_{MC} = 100,000$.

was chosen as $N_{MC} = 10,000$. Based on the interpretation of these results and in particular from Fig. 4, an inverse relationship between the CoV and the bias with the number of integration points was noticed. The selection $N_{MC} = 10,000$ satisfied the accuracy condition for both aspects with reasonably reduced tolerance and confidence bounds (less than one percent difference in comparison with the CF value). Even though a reduction of CoV was observed for $N_{MC} > 10,000$, the relative benefit did not seem to warrant an increment of computational time (Table 3).

Two other structures (100 m and 180 m tall) were also used for numerical validation. Even though results were omitted for brevity, similar results were obtained for the same number of N_{MC} . The latter results are compatible with the observation that the quantity $E[\hat{f}(n, z_1, z_2)]$ in Eq. (5) appears to be marginally affected by the size of the interval of integration, i.e., independent of height because of a subsequent normalization of the Z_A and Z_B integration variables in Eq. (5).

Therefore, the value $N_{MC} = 10,000$ was employed in Section 5 and extended to both steps of the numerical MC procedure. It must be noted, however, that the criterion for “optimal” selection was not based on a rigorous solution to a minimization problem, associated with the above-described indicators. In contrast, this choice was primarily derived from the analysis of the numerical results in Tables 2 and 3 and for a limited number of N_{MC} values. Therefore, the proposed value of $N_{MC} = 10,000$ can be accepted for the implementation of the algorithm in the case of the CAARC building, even though it requires careful interpretation before an extension to a wider set of applications.

5. Implementation of the two-step MC algorithm

5.1. “Fragility analysis”

The two-step MC algorithm was employed in this section as a numerical tool in an attempt to simulate the fragility analysis of the CAARC prototype building under the influence of wind loading. Fragility analysis is a standardized methodology, utilized for performance-based structural analysis against wind hazards [6,13,40]. The objective of a fragility analysis is the computation of the conditional probability of exceedance of representative indicators (maximum lateral drift, peak acceleration levels, etc.), corresponding to a specific feature of the dynamic response. A set of thresholds is usually defined (or derived) to represent different

levels of structural performance based on such indicators, which may be selected by the designer.

“Fragility curves” were derived from the numerical estimation of the probability associated with the exceedance of pre-selected thresholds representing the along-wind dynamic response, using the proposed algorithm. In this study, exceedance probabilities were represented as a function of the mean wind velocity V_z at $z = h$, which was related to buffeting response perpendicular to the “D – h” face of the prototype CAARC building (Sections 3 and 4). The simulations incorporated the effects of uncertainty in the description of the aerodynamic loading.

Cumulative probabilities were used to derive the structural response fragility (F_T), i.e., to find the probability (P) of a generic random variable X (e.g., top-floor RMS response) exceeding a pre-selected threshold T , conditional on the presence of a wind storm with $V_z = \bar{U}(h)$ at $z = h$, as

$$F_T(V_z) = P[X > T | V_z = \bar{U}(h)]. \quad (7)$$

In the numerical derivation of Eq. (7), the effects of random aerodynamic static coefficients and random exponential decay coefficients were analyzed. Specifically, emphasis was given to the drag coefficient, C_D , and the exponential coherence coefficient, C_z in Eqs. (1)–(4) while uncertainty arising from other aerodynamic coefficients or other sources (e.g., structural damping) was not analyzed. Two investigations were conducted: the randomization of C_D in Eq. (1), and the concurrent randomization of C_D and C_z in the same equation. The randomization of such parameters reflects the presence of measurement errors in the wind tunnel tests, in an attempt to replicate the differences among various laboratories described in [37]. The objective of this investigation was the analysis of the algorithmic performance of the proposed MC procedure (Steps 1 and 2).

Fig. 5 shows typical probability density function (PDF) plots of the analyses conducted on the CAARC prototype building, at the reduced velocity $\bar{U}(h)/(n_0 B) = 8.2$, referenced at $z = h$. Fig. 5(a) analyzes the effects of a random static drag coefficient per unit height, assumed as a constant throughout the height, and simulated as a gamma-type random variable with mean 1.0 and standard deviation 0.3. Fig. 5(b) shows the PDF of the top-floor RMS response, σ_x , based on the simulations conducted for a random C_D only. As expected, due to the linear dependence between C_D and modal force (Eq. (1)), the response PDF (Fig. 5(b)) also follows a gamma distribution. In each sub-figure, the curve labeled “probabilistic model” refers to the PDF calculated from the pre-selected values for mean (1.0) and standard deviation (0.3), while the curve labeled “MC-based PDF” was derived from the numerically generated histogram.

Two examples of fragility curves for an uncertain distribution of C_D and for a combination of random C_D and C_z are shown in Figs. 6 and 7, respectively, as a function of reduced velocity $U(h)/(n_0 B)$. Fig. 6(a) shows the top-floor along-wind RMS response, which corresponds to Fig. 5 when $U(h)/(n_0 B) = 8.2$. Fig. 6(b) shows the along-wind peak response derived from Fig. 5(a) by application of Davenport’s peak factor equation [10,41]. The interval of reduced velocities is variable between 4 and 10, which coincides with medium to severe wind velocities for the CAARC prototype response between 25 and 60 m/s at $z = h$. Fig. 7(a,b) are similarly described. In both figures, a “spline” function was used to connect the simulated points, indicated by solid markers.

In both Figs. 6 and 7 the dimensional displacement thresholds used in this study (T1 to T5) were defined as a function of the building width, variable between $0.10\%B$ and $1.50\%B$ ($B = 30.5$ m). These thresholds, listed in Table 4, were selected as a first attempt at defining appropriate and realistic limit states. For example, if threshold T5 was associated with a maximum lateral drift criterion,

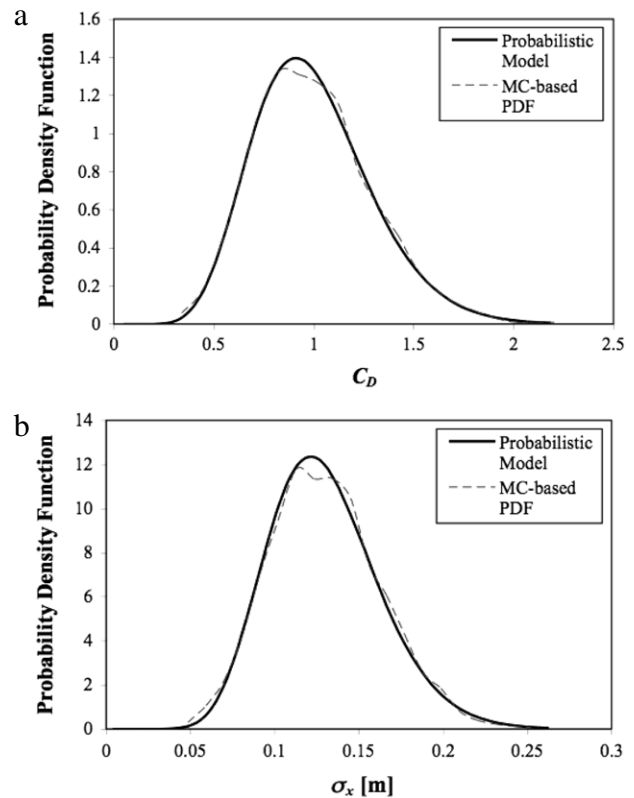


Fig. 5. Results of MC algorithm (Step 2) for gamma-type random distribution of the drag coefficient (C_D) only – (a) C_D PDF; (b) σ_x PDF for $\bar{U}(h)/(n_0 B) = 8.2$.

Table 4

Thresholds for use in the fragility analysis of the CAARC building.

Label	Threshold level (m)
T1	$0.10\%B = 0.031$
T2	$0.25\%B = 0.076$
T3	$0.50\%B = 0.153$
T4	$1.00\%B = 0.305$
T5	$1.50\%B = 0.458$

acceptable in the context of wind-induced dynamic analyses of a full-scale building [42], it would also correspond to an inter-story drift ratio of 1/400 for the CAARC building [42].

From the analysis of the figures it can be seen that if the dynamic RMS vibration is employed as a measure of performance and T5 is selected as a reference threshold, the probability of exceedance is low, below 1% even during severe wind conditions. However, if the peak response is used, which also includes the effects of the mean drift, F_T is large, equal to about 90% at $\bar{U}(h)/(n_0 B) = 8.2$. This fact may possibly lead to unacceptable drift ratios, which appear in this example to be predominantly associated with the mean wind pressure and force distribution.

Furthermore, from the comparison of Fig. 7 with Fig. 6 there appears that the contribution of a random C_z to the F_T curve is marginal as opposed to the influence of C_D . However, this fact may be related to this simplified model and the result may not be applicable to more realistic buildings.

Finally, even though this example suggests a predominant effect by the static wind load on the probability of exceedance for the CAARC building, the contribution of the structural dynamic response and of σ_x cannot be ruled out for other tall flexible structures and should be possibly incorporated in the response estimation against high winds.

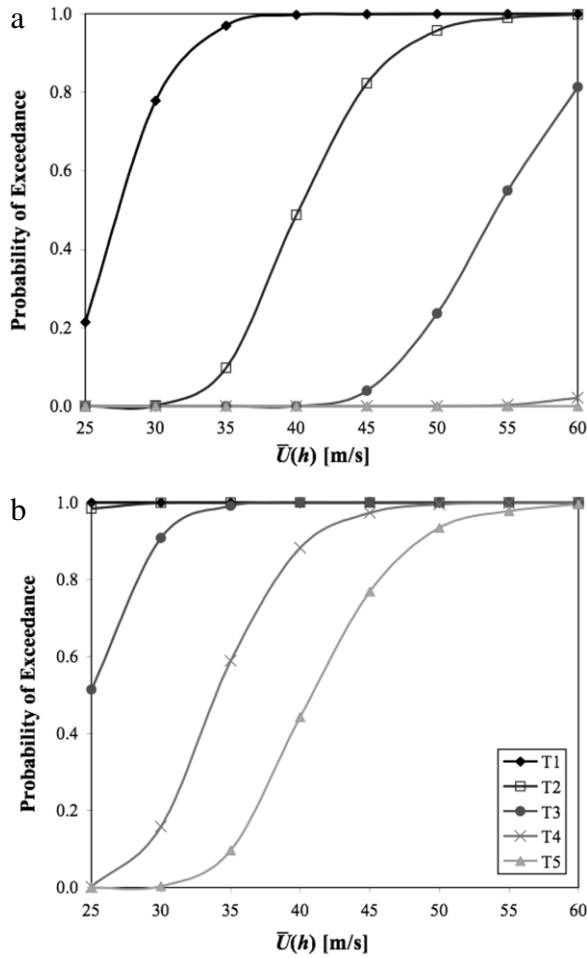


Fig. 6. Example of structural fragility curves for uncertain distribution of C_D as a function of the reduced velocity, $\bar{U}(h)/(n_0 B)$ – (a) along-wind RMS response; (b) peak response. Note: T1 to T5 are dimensional pre-selected exceedance thresholds, which are the same for both figures ($B = 30.5$ m, see Fig. 2).

5.2. Exploratory performance assessment

A preliminary example of a performance-based assessment is presented in this section for illustration purposes. The objective of this preliminary analysis was to provide an example of vulnerability assessment of a tall building subjected to wind hazards and located near Boston, Massachusetts, USA, similar to the CAARC building. In general, the computation of the probability (P_T), indicating the cumulative “performance loss” for all possible mean wind speed levels, is required. The quantity P_T was determined by convolving the structural fragility curves $F_T(V_z)$, associated with a given threshold T as a function of mean wind speed V_z and derived as in Section 5.1, with the wind speed hazard curve f_{V_z} [17]:

$$P_T = \int_0^{\infty} F_T(V_z) f_{V_z}(V_z) dV_z. \quad (8)$$

In Eq. (8), f_{V_z} is the probability density function (PDF) of the reference wind speed [17]. In the first part of this investigation full-scale records were used to find $f_{V_z}(V_z)$. Wind data from a buoy off the coast of Boston, Massachusetts, which is part of the NOAA (National Oceanic and Atmospheric Administration) system (NOAA Station 44013, 42.346 N 70.561 W), was utilized [43]. Wind speeds (8-min averaging time) are continuously recorded using an anemometer located 5 m above the site elevation. Wind directionality effects were neglected at this stage.

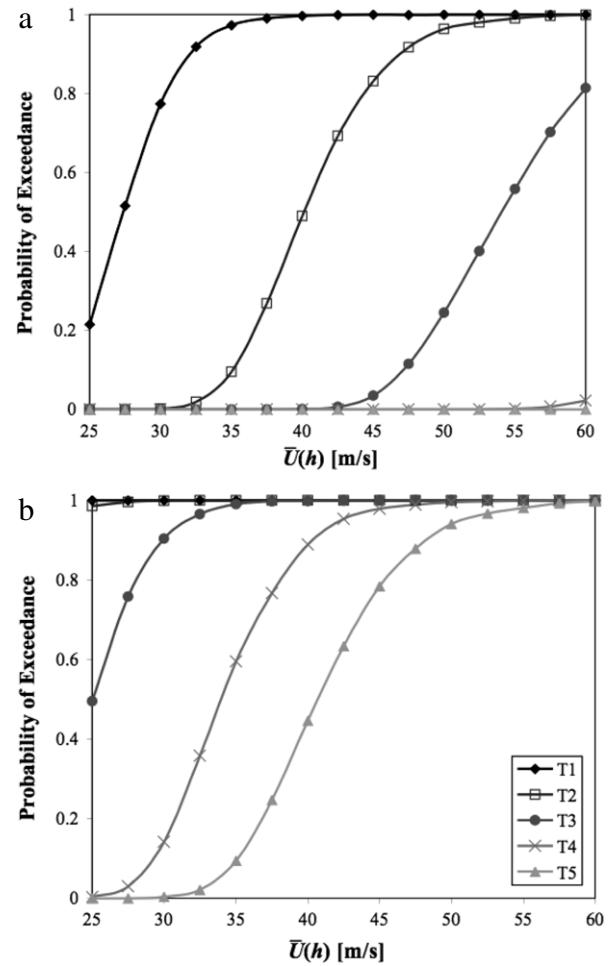


Fig. 7. Example of structural fragility curves for uncertain distributions of C_D and C_z as a function of the reduced velocity, $\bar{U}(h)/(n_0 B)$ – (a) along-wind RMS response; (b) peak response. Note: T1 to T5 are dimensional pre-selected exceedance thresholds, which are the same for both figures ($B = 30.5$ m, see Fig. 2).

This investigation considered two data sets: “continuous data” and “peak data”. The “continuous data” set was based on a record from a single year (2008) in which readings were recorded every 10 min, and the “peak data” set was derived from yearly maxima velocities over a 25-year period (1984–2008). The original wind speed data were rescaled to obtain equivalent 10-min wind speeds [35], which are used by the algorithm Eqs. (1)–(4) and (8). Furthermore, the logarithmic law and dependent relationships were employed to relate the measured open-sea wind data to an urban terrain [35] and to derive the mean wind speed profile at the top of the building ($z = h$) using two roughness lengths, $z_0 = 0.002$ m (sea surface type, representative of a site in the proximity of the shore) and $z_0 = 0.100$ m (urban exposure) [44].

Table 5 summarizes the results of the site wind analysis. The measured wind data were also compared to the ASCE-7 2005 design wind speed [45] for the coastal region of Massachusetts, which prescribes a 3-s gust value of 49 m/s (at an elevation of 10 m), corresponding to 10-min wind speed of 33.8 m/s.¹ Results in Table 5 confirm that the design wind speeds derived from [45], projected at an elevation $z = h$, were compatible with the

¹ The ten-minute wind speed was based on ASCE-7 2005 three-second gust speed, since at the time of submission of this study the latter standard was officially recognized. Differences may be possible in comparison with the most recent ASCE-7 Standard, published in 2010.

Table 5

Wind speeds derived from buoy data [43] and ASCE 7–05 as a function of roughness length.

Wind speed	$z_0 = 0.002$ m		$z_0 = 0.100$ m	
	Continuous data	Peak data	Continuous data	Peak data
Minimum (data) (m/s)	0.0	25.2	0.0	21.8
Maximum (data) (m/s)	26.8	36.8	23.2	31.9
Design (ASCE 7–05) (m/s)	–	56.6	–	49.1

Table 6

Weibull and Gumbel distribution parameters.

Distribution parameters	Weibull distribution (Continuous data)	
	$z_0 = 0.002$ m	$z_0 = 0.100$ m
Scale parameter	8.99	7.79
Shape parameter	2.15	2.15
Distribution parameters	Gumbel distribution (Peak data)	
	$z_0 = 0.002$ m	$z_0 = 0.100$ m
Scale parameter	2.45	3.23
Location parameter	27.64	36.35

measured wind data, which were subsequently utilized in the analyses.

A Weibull distribution [35] was employed to describe the continuous data, representative of the marginal wind velocity distribution with day-to-day values that a building can experience; these also include “near zero” winds. The peak data, obtained from the 25-year period, was fitted to an Extreme Value Type I (Gumbel) distribution, chosen to represent the behavior of the annual peaks, i.e., of extreme storms. Table 6 summarizes the distribution parameters that were used to describe the PDFs of the wind speed for both data sets.

In the second part of this investigative example, the $F_T(V_z)$ curves of the top-floor along-wind RMS and peak responses Fig. 7, determined in Section 5.1 for the prototype CAARC building with $V_z = \bar{U}(h)$, were combined with the velocity PDFs derived in Tables 5 and 6 to numerically estimate P_T in Eq. (8). Application to human comfort/occupancy conditions and potential damage to secondary non-structural systems, affected by lateral drift values, was considered. In terms of human comfort and occupancy, the $F_T(V_z)$ curves of the RMS response might be related to human tolerance (smaller-magnitude persistent effects), whereas the curves of the peak dynamic response could be seen as a descriptor of instantaneous human perception (i.e., an extreme feeling for “immediate occupancy”) [27]. In terms of damage to the secondary, non-structural building systems, the RMS response could be related to, for example, a malfunctioning of sensitive equipment installed on the external façade, while the peak response could be of concern for elements predisposed to failure under sudden and large-amplitude vibration.

Combinations of the three response configurations and the two sets of wind data were used to calculate the probability P_T (Eq. (8)), as indicated in Table 7. A total of six cases were investigated. These must be interpreted as examples to illustrate the features of the algorithm for this particular example; therefore, they cannot be used as general guidelines.

Case 1 is the combination of the RMS response with the continuous wind data and analyzes levels of human tolerance or predicts a downtime of sensitive equipment. Case 2 combines the RMS response with the peak wind data and is related to non-structural elements, which could be damaged or affected by progressive deterioration under repeated small-amplitude vibration under a severe storm (i.e., a larger wind velocity). Lastly, Case 3 combines the peak response with the peak wind data, which pertains to acute human discomfort under more severe winds, for example, leading to temporary loss of safe occupancy. Case

3 might also be used to describe vibration levels causing sudden (as opposed to progressive) damage to secondary non-structural elements (i.e., large windows on the façade).

Table 8 summarizes the results of the performance analysis based on the formerly described cases for a given threshold from T1 to T5, defined in Section 5.1. In Table 8 the mean recurrence interval (MRI) is presented for thresholds T1 to T5 and for each of the response/wind cases, from 1a to 3b. The estimation of the MRI was based on the assessment of the performance loss in terms of probability P_T (Eq. (8)) for each case and was independently assessed for thresholds T1 to T5. The MRI values corresponding to an exceedance probability less than 0.1% were not included in the table since the estimated P_T was below the numerical resolution of the algorithm, which depends on the initial selection of N_{MC} .

In Table 8 cases 1a and 1b relate to a reference duration period of 10 min, i.e., utilize the marginal distribution of the mean wind velocity recorded on average every year. In contrast, cases 2a through 3b can be associated with an annual P_T , since the peak distribution of the mean wind velocity was employed to determine the MRI. As an example, if threshold T1 were selected in conjunction with Case 1b, the building would exceed T1 approximately every 7 months. For the same case, larger thresholds, e.g., T3 through T5, are not likely to ever be exceeded. Threshold T5, which is comparable to the maximum lateral drift for the CAARC building, as indicated in Section 5.1, is not likely to be exceeded for any wind hazard case, except for Case 3a with an MRI of approximately 1100 years.

It must be noted that, however, the MRI for Cases 1a and 1b in Table 8 is either very low or cannot be numerically estimated, under the given assumptions on F_T , $f_{V_z}(V_z)$ and N_{MC} . This result could have been certainly anticipated without conducting a full performance analysis, since the annual probability of exceedance for Cases 1a and 1b is mostly influenced by the short duration of the records (i.e., the marginal probability of V_z , corresponding to one sample every 10 min) rather than the actual thresholds, except for T1. Nevertheless, Cases 1a and 1b were retained in Table 8 and in the discussion for the purpose of illustrating the general features of the algorithm.

Finally, the analysis of Table 8 suggests that the original pre-selected thresholds could possibly be increased, since the MRI consistently exceeded the 700-year return period, commonly utilized for extreme events (excluding hurricane winds), even for a performance objective level corresponding to a drift ratio of 1/400.

6. Summary and conclusions

This study summarizes preliminary research activities aiming at the development of a performance-based methodology for estimation of the response of high-rise buildings against wind hazards. A numerical “two-step Monte Carlo (MC) algorithm” was proposed for deriving the dynamic response in the frequency domain, accounting for uncertainty and measurement errors. The simulation algorithm was employed to analyze the effects of uncertain wind force estimation on the dynamic response of a simulated tall building, modeled after the CAARC benchmark building. Linear along-wind dynamic response under stationary wind with dynamic modal superposition, restricted to the fundamental bending mode, was considered.

Table 7

Description of wind cases employed in the performance analysis.

Case	Description of case		Wind data	z_0 (m)
	Type of response	Distribution type		
1a	RMS response	Marginal velocity	1-year continuous data	0.002
1b	RMS response	Marginal velocity	1-year continuous data	0.100
2a	RMS response	Annual peak velocity	25-year peak data	0.002
2b	RMS response	Annual peak velocity	25-year peak data	0.100
3a	Peak response	Annual peak velocity	25-year peak data	0.002
3b	Peak response	Annual peak velocity	25-year peak data	0.100

Table 8

Mean recurrence interval of a wind event, derived from the probability of performance loss and based on full-scale wind data (near Boston, Massachusetts, USA), for vibration thresholds from T1 to T5 of the CAARC building.

Case	Mean recurrence interval (in years)				
	T1	T2	T3	T4	T5
1a	0.3	1264.5	–	–	–
1b	0.6	16043.4	–	–	–
2a	2.5	2228.9	–	–	–
2b	10.3	–	–	–	–
3a	1.2	1.2	1.7	24.0	1123.3
3b	2.5	2.5	4.8	450.5	–

Note: The dash marker (‘–’) in this table indicates that the calculated probability is equal to zero, i.e., below the accuracy/resolution of the numerical integration algorithm, corresponding to a practically unreasonable mean recurrence interval.

In the first part of the study, validation of the numerical procedure was carried out by comparing the simulated results to the reference values derived from wind tunnel tests in the literature. In the second part, the algorithm was employed to derive fragility curves associated with serviceability limit states and related to maximum lateral drift; five thresholds, associated with maximum drift ratios ranging from almost unperceivable values to 1/400 of the total building height, were considered. In the last part of the study, preliminary structural performance assessments were conducted for the simulated 183 m building located near Boston, Massachusetts, USA. Mean recurrence intervals, associated with serviceability limit states and dictated by the selection of the above-described performance thresholds, were calculated.

The results of this study demonstrated the adequacy of the proposed algorithm and showed promising potential of the “two-step MC algorithm” towards an application to more realistic examples. Even though the first step of the algorithm, employed for estimating the power spectral density of the generalized modal force, could be replaced by equivalent simplified estimation formulas for tall buildings [31,34,46], which utilize an approximate solution of the modal force and response spectra for the prediction of the dynamic response, the proposed algorithm has the potential advantage of allowing for further generalization. For example, aspects such as bi-directional modal coupling and the influence of higher modes, which are marginally contemplated by the simplified estimation formulas, could be readily incorporated.

Future investigations should include more rigorous structural analysis techniques, and possibly account for the across-wind and torsional responses in addition to the along-wind response. An analysis using higher vibration modes would be desirable for the assessment of comfort criteria in very tall buildings [47]. Finally, future studies might also be directed towards the extension of the proposed algorithm to the analysis of accelerations and vibrations during extreme events, not only related to occupant comfort.

Acknowledgements

The study period of MAS was supported in part by Northeastern University, Department of Civil and Environmental Engineering.

LC would like to acknowledge the partial support of the National Science Foundation CAREER Award, CMMI 0844977 (2009–2014). The study, described in this paper, constitutes a preliminary investigation on computer-based estimation of wind loading on buildings, which is being considered as part of the current and future research activities. Any opinions, findings, conclusions or recommendations expressed in this study are those of the authors and do not necessarily reflect the views of any agency or institution mentioned above.

References

- [1] Inokuma A. Basic study of performance-based design in civil engineering. *J Profess Issues Eng Education Practice* 2002;30–5.
- [2] Ellingwood B, Rosowsky D, Li Y, Kim JH. Fragility assessment of light-frame wood construction subjected to wind and earthquake hazards. *J Struct Eng* 2004;129:1–30.
- [3] Rosowsky D, Ellingwood B. Performance-based engineering of wood frame housing: fragility analysis methodology. *J Struct Eng* 2002;32–8.
- [4] NBSIR. Performance criteria resource document for innovative construction. Report NBSIR 77-1316. Washington, DC: National Bureau of Standards; 1977.
- [5] Ellingwood B. LRFD: implementing structural reliability in professional practice. *Eng Struct* 2000;22:106–15.
- [6] Norton T, Abdullah M, Stephens D. Proposed methodology for performance-based vulnerability assessment of wind-excited tall buildings. In: Fourth international conference on “Advances in wind and structures – AWAS 08”. p. 1228–46.
- [7] SEAOC. Vision 2000 – A framework for performance based earthquake engineering. Structural Engineers Association of California; 1995.
- [8] SEAOC. Recommended lateral force requirements and commentary, 7th ed., Structural Engineers Association of California; 1999.
- [9] Davenport AG. Response of supertall buildings to wind. In: Third international conference on tall buildings. p. 705.
- [10] Davenport AG. Response of six building shapes to turbulent wind. *Phil Trans Roy Soc London Ser A* 1971;269(1199):385–94.
- [11] Kareem A. Dynamic response of high-rise buildings to stochastic wind loads. *J Wind Eng Ind Aerodyn* 1992;41–44:1101–12.
- [12] Kareem A. Model for predicting the acrosswind response of buildings. *Eng Struct* 1984;6(2):136–41.
- [13] Bashor R, Kareem A. Probabilistic performance evaluation of buildings: an occupant comfort perspective. In: 12th international conference on wind engineering (12-ICWE). 2007. p. 1335–42.
- [14] Bracci JM. Performance-based design of concrete building for wind loads (ACI SP-240-1). Publication SP-240. Farmington Hills, Michigan, USA: American Concrete Institute; 2006.
- [15] Jain A, Srinivasan M, Hart GC. Performance based design extreme wind loads on a tall building. *Struct Design Tall Build* 2001;10(1):9–26.
- [16] Ellingwood B, Tekie PB. Wind load statistics for probability-based structural design. *J Struct Eng* 1999;453–63.
- [17] Li Y, Ellingwood B. Hurricane damage to residential construction in the US: importance of uncertainty modeling in risk assessment. *Eng Struct* 2006;28:1009–18.
- [18] Bashor R, Kareem A. Load factors for dynamically sensitive structures. In: 11th Americas conference on wind engineering. 2009. CD-ROM.
- [19] Robert CP, Casella G. Monte Carlo statistical methods. New York: Springer Science; 2004.
- [20] Grigoriu M. Stochastic calculus. In: Applications in science and engineering. Boston, MA, USA: Birkhäuser; 2002.
- [21] Tempo R, Calafiore G, Dabbene F. Randomized algorithms for analysis and control of uncertain systems. London, UK: Springer-Verlag; 2005.
- [22] Tse KT, Hitchcock PA, Kwok KCS. Mode shape linearization for HFFB analysis of wind-excited complex tall buildings. *Eng Struct* 2009;31(3):675–85.
- [23] Chen X, Kareem A. Validity of wind load distribution based on high frequency force balance measurements. *J Struct Eng* 2005;131(6):984–7.
- [24] Holmes J, Rofail A, Aurelius L. High frequency base balance methodologies for tall buildings with torsional and coupled resonant modes. In: 11th international conference on wind engineering. Lubbock (TX, USA): Texas Tech University, June 2–5; 2003. p. 2381–88.
- [25] Zhou Y, Kareem A, Gu M. Mode shape corrections for wind load effects. *J Eng Mech* 2002;128(1):15–23.

- [26] Bashor R, Kijewski-Correa T, Kareem A. On the wind-induced response of tall buildings: the effect of uncertainties in dynamic properties and human comfort thresholds. In: 10th Americas conference on wind engineering. 2005. CD-ROM.
- [27] Kijewski-Correa T, Pirnia D. "Pseudo-full-scale" evaluation of occupant comfort in tall buildings. In: 11th Americas conference on wind engineering. 2009. CD-ROM.
- [28] Burton MD, Kwok KCS, Hitchcock PA, Denoon RO. Frequency dependence of human response to wind-induced building motion. *J Struct Eng* 2006;296–303.
- [29] Kwok KCS, Hitchcock PA. Occupant comfort test using a tall building motion simulator (keynote paper). In: Fourth international conference on "Advances in wind and structures - AWAS 08". p. 87–99.
- [30] Tse KT, Kwok KCS, Hitchcock PA, Samali B, Huang MF. Vibration control of a wind-excited benchmark tall building with complex lateral-torsional modes of vibration. *Adv Struct Eng* 2007;10(3):283–304.
- [31] Piccardo G, Solari G. Generalized equivalent spectrum technique. *Wind Struct* 1998;1(2):161–74.
- [32] Humar JL. Dynamics of structures. London: Taylor & Francis; 2002.
- [33] Tallin A, Ellingwood B. Wind induced lateral-torsional motion of buildings. *J Struct Eng* 1985;111(10):2197–213.
- [34] Kareem A. Aerodynamic response of structures with parametric uncertainties. *Struct Safety* 1988;5(3):205–25.
- [35] Simiu E, Scanlan RH. Wind effects on structures. New York: John Wiley & Sons, Inc; 1996.
- [36] Caracoglia L. Influence of weather conditions and eccentric aerodynamic loading on large amplitude aeroelastic vibration of highway tubular poles. *Eng Struct* 2007;29:3550–66.
- [37] Melbourne WH. Comparison of measurements on the CAARC standard tall building model in simulated model wind flows. *J Wind Eng Ind Aerodyn* 1980;6(1–2):73–88.
- [38] Dyrbye C, Hansen SO. Wind loads on structures. New York: John Wiley & Sons, Inc; 1997.
- [39] Walpole R, Myers R, Myers S, Ye K. Probability and statistics for engineers and scientists. Upper Saddle River, NJ: Prentice Hall; 2002.
- [40] Filliben JJ, Gurley K, Pinelli J-P, Simiu E, Subramanian C. Fragility curves, damage matrices, and induced loss estimation. In: Third international conference on computer simulation in risk analysis and hazard mitigation. 2002. p. 119–26.
- [41] Davenport AG. Note on the distribution of the largest value of a random function with application to gust loading. *Proc Inst Civil Eng* 1964;28:187–96.
- [42] Chan CM, Chui JKL, Huang MF. Integrated aerodynamic load determination and stiffness design optimization of tall buildings. *Struct Design Tall Special Build* 2007;18(1):59–80.
- [43] NOAA. National Oceanic and Atmospheric Administration, Station 44013 – BOSTON 16 NM East of Boston, MA. http://www.ndbc.noaa.gov/station_page.php?station=44013.
- [44] Tieleman H. Roughness estimation for wind-load simulation experiments. *J Wind Eng Ind Aerodyn* 2003;91:1163–73.
- [45] ASCE. Minimum design loads for buildings and other structures (7-05). Reston, VA: American Society of Civil Engineers, 2005.
- [46] Solari G. Equivalent wind spectrum technique: theory and applications. *J Struct Eng* 1988;114(6):1303–23.
- [47] Irwin PA. Wind engineering research needs, building codes and project specific studies. In: 11th Americas conference on wind engineering; 2009. CD-ROM.